MJO-related intraseasonal variation of gravity waves in the southern hemisphere subtropical stratosphere revealed by high-resolution AIRS observations

Chikara Tsuchiya[1,4], Kaoru Sato[1], M. Joan Alexander[2], and Lars Hoffmann[3]

Key points

- Intraseasonal variability of gravity waves in the middle stratosphere was examined.
- The gravity waves are synchronized with the MJO in the austral summer subtropics.
- The MJO likely modulate the gravity waves in two ways, i.e., generation and propagation.

Corresponding author: C. Tsuchiya, Department of Earth and Planetary Science, University of Tokyo, Science Building 1, 7-3-1 Hongo, Bunkyo-ku, Tokyo, 113-0033, Japan. (chikara@eps.s.utokyo.ac.jp)

[1]Department of Earth and Planetary Science, University of Tokyo, Tokyo, Japan.

[2]NorthWest Research Associates, CoRA Office, Boulder, Colorado, USA.

[3]Juelich Supercomputing Centre Forschungszentrum Juelich 52425 Juelich, Germany.

[4]Now at Japan Coast Guard, Tokyo, Japan.

Abstract. The intraseasonal variability of gravity waves (GWs) in the austral summer middle stratosphere was examined using dedicated high-resolution temperature retrieval from the Atmospheric Infrared Sounder data. Composite maps were made of stratospheric GW temperature variances, large-scale zonal winds around the tropopause, and precipitation based on the real-time multivariate Madden-Julian Oscillation (MJO) index. Regional distributions of these quantities are synchronized with the MJO: The GW variances are larger for stronger precipitation, and for more strongly westward wind around the tropopause at a given precipitation. These results suggest that the GWs observed by AIRS in the stratosphere originate from convection. Moreover, it is shown that the zonal wind around the tropopause likely controls the GW propagation into the stratosphere by a critical level filtering mechanism. This means that the MJO can modulate the middle atmospheric circulation by regulating the GWs in two ways, namely, generation and propagation.

1. Introduction

Recent previous studies using high resolution temperature data from satellites such as the Microwave Limb Sounder (MLS) and HIgh Resolution Dynamics Limb Sounder (HIRDLS) and from simulation by gravity-wave (GW) resolving general circulation models (GCM) indicate that GW activity is high in the summer subtropics [*McLandress et al.*, 2000; *Jiang et al.*, 2004; *Sato et al.*, 2009; *Wright and Gille*, 2011]. It is considered that such GWs originate from vigorous convection based on similarity of regional distributions. GWs in the summer subtropics are important for driving the residual mean circulation not only in the mesosphere but also in the stratosphere. In particular, GWs are important drivers of the summer-hemispheric part of the winter cell of the Brewer-Dobson circulation where stationary planetary waves cannot propagate upward into the westward background wind [*Okamoto et al.*, 2011]. Data from the Atmospheric Infrared Sounder (AIRS) having high horizontal resolution has been used to examine convectively generated GWs with relatively small horizontal wavelengths and long vertical wavelengths in the stratosphere as radiance perturbations [*Wu et al.*, 2006; *Kim et al.*, 2009; *Hecht et al.*, 2009; *Grimsdell et al.*, 2010; *Hoffmann and Alexander*, 2010; *Yue et al.*, 2013].

It is well known that large-scale convective systems in the tropics migrate eastward as the Madden-Julian Oscillation (MJO) with 30–60 day time periods [*Zhang*, 2005] and a characteristic regional distribution. Although convection is an important source of GWs, few studies have focused on the relation between GWs and convection systems in terms of spatiotemporal variation on such intraseasonal time scales. Thus, in the present study, the intraseasonal variation of GWs in the middle stratosphere is examined in terms of the regional distribution using recently-retrieved high-resolution temperature data from AIRS observations [*Hoffmann and Alexander*, 2009]. The precipitation at the ground is used as an index of the convection activity. Gravity waves in the tropics can vary as the El Nino-Southern Oscillation with interannual time scales. This issue will be examined in a companion paper [*Sato et al.,* submitted to J. Geophys. Res., hereafter referred to as STAH15].

By using a high-resolution general circulation model resolving GWs explicitly without any GW parameterizations [*Watanabe et al.*, 2008], *Sato et al.* [2009] examined GWs in a meridional cross section covering altitudes from the ground to the upper mesosphere with fine vertical resolution. This model succeeded in simulating realistic dynamical fields in the middle atmosphere and hence the simulated wave fields (including GWs) could be analyzed as surrogates of the real atmosphere. *Sato et al.* [2009] showed that GWs are dominant in the subtropical monsoon region in the lower stratosphere, and they likely originate from vigorous convection. They also indicated that strong westward winds in the monsoon region at the tropopause level are important for the penetration of GWs into the middle atmosphere. Thus, the zonal winds at 100 hPa, roughly corresponding to the tropopause, are also examined in relation to the GW activity observed by the AIRS.

In Section 2, the data used in the present study and the analysis methods are described. Intraseasonal variations of GW variances in the middle stratosphere are examined in terms of the MJO in Section 3. In Section 4, results are summarized and concluding remarks are made.

2. Data and method of analysis

AIRS [*Aumann et al., 2003*] measures thermal emissions of atmospheric constituents with hyperspectral resolution (2378 channels). The footprint size is 13.5 km at nadir and 39.6 km at its edge, and the scan interval along the satellite orbit is 18 km at nadir. AIRS scans across the track with a horizontal distance of 1765 km on the ground [*Hoffmann* *et al.*, 2013]. In the present study, new temperature retrieval data with the AIRS native horizontal resolution [*Hoffmann and Alexander*, 2009] are used. Note that the AIRS operational temperature retrieval data have a coarser horizontal resolution by a factor of 3×3 compared to this high-resolution retrieval. As a larger number of 4.3 and 15 μm channels were used to retrieve the temperature during nighttime [*Hoffmann and Alexander*, 2009], the signal-to-noise ratio is higher for nighttime than for daytime measurements. Thus, we used only data in the nighttime when the solar elevation angle is less than −20°. In addition, as the retrieval noise is lowest at altitudes of 25–45 km [*Hoffmann and Alexander*, 2009], we mainly focus on data at an altitude of 39 km, approximately corresponding to 3 hPa. The vertical resolution of the retrieval is about 9 km at that level. It may be worth noting here that the GW characteristics around 3 hPa by the AIRS high-resolution retrieval data were consistent with the simulation by the GW resolving general circulation model [*Watanabe et al.*, 2008; *Sato et al.*, 2009] in terms of the magnitude and horizontal distribution of GW variances when an observational filter for the AIRS measurement was taken into account (not shown).

Global Precipitation Climatology Project (GPCP) version 1.2 data [*Huffman et al.*, 2001] are used to analyze precipitation as an indicator of convective activity. We also use daily-mean data from the Modern Era Retrospective Analysis for Research and Applications (MERRA) [*Rienecker et al.*, 2011] to examine the background wind field through which the GWs propagate. The real-time multivariate MJO (RMM) index[1] [*Wheeler and Hendon*, 2004] is used to see the variation of the horizontal distribution of MJO precipitation and

[1] The time series of the RMM index obtained using the NCEP operational data are provided at the site "http://cawcr.gov.au/staff/mwheeler/maproom/RMM/"

synchronization with GW variances.

The GW temperature fluctuations are extracted from the AIRS temperature retrieval by subtracting a large-scale temperature field from the original data. The large-scale temperature field is obtained by a regression of the original temperature data onto a second-order polynomial function across the track, and by applying a running mean with a length of 31 grid points along the track. Considering the footprint size described above, the large-scale temperature field obtained in this way have horizontal scales greater than about 550 km.

Next the GW amplitudes and horizontal wavelengths are estimated by applying an S-transform [*Stockwell et al.*, 1996] to two adjacent data scans along the satellite orbit [*Alexander and Barnet*, 2007]. From the signal with the highest covariance in the S-transform spectra, the horizontal wavelengths, the direction of horizontal wavenumber vector, and the squared temperature amplitudes (hereafter referred to as GW variances) are obtained. A similar perpendicular analysis was performed on adjacent rows of data along the satellite orbit. Among these two sets of wave parameter estimates obtained from the S-transform analyses for the data series along the orbit and from that for the data series across the orbit, we retained those wave parameters for which the angle between the horizontal wavenumber vector and the direction of data series is smaller. Horizontal wavelengths which can be detected in this way are in the range of 50−700 km. It was also seen from the power spectra derived from data without any GW events that noise of this new retrieval data is mainly distributed in the horizontal wavelength range shorter than 70 km [STAH15]. To further reduce the effects of noise, we did not include the data in the analysis when and where the background wind at 3 hPa was weaker than 10 m s^{-1}, since it is expected that the majority of GWs in such conditions have vertical wavelengths too short to be detected by AIRS. It was confirmed that this exclusion has little effect on the GW variance distribution that will be shown in later sections. See STAH15 for more details of the analysis.

The analyzed time period is December to March of 2003-2011 when the MJO is dominant. The analysis is focused on the Southern Hemisphere (SH) subtropical region where GW variance is significantly large in the austral summer. Mean GW variance and precipitation were obtained at respective bins of 2.5° latitude and 10° longitude.

3. Results

We first investigate the characteristics of the GW variance around 3 hPa on intraseasonal time scales from 10 days to several tens of days as a function of time and longitude. Figures 1a and 1b respectively show the longitude-time sections of the precipitation and the GW variance around 3 hPa, averaged for latitudes of 0°–20°S, in the austral summer from December to March of each year. The zonal wind at 100 hPa is also shown with contours in Figure 1b. It is clear in Figure 1a that the regions where precipitation is greater than 8 mm day^{-1} move eastward. This eastward propagation of the precipitation regions is associated with the MJO. An interesting feature is that the regions with GW variance greater than 0.9 K^2 similarly propagate eastward, especially in the longitude region of about 60°E–120°W. It is also worth noting that the zonal wind at 100 hPa is westward in the regions where the large GW variance was observed, and that the GW variance is small where the zonal wind is weak or eastward (Figure 1b). The zonal wind contour of 5 m s^{-1} seems to trace the eastern edge, i.e., the forefront of the large GW variance region at east longitudes to the west of the dateline. This feature suggests that the zonal wind at 100 hPa strongly affects upward propagation of GWs.

At each longitude, correlation coefficients between the time series of the precipitation and the GW variance were calculated (Figure 2a). The 99% confidence level is a correlation of 0.27, which is shown by a solid line. The correlation is statistically significant in the longitudes of 20°E–130°W, where both precipitation and GW variance are large. A regression coefficient of the GW variance to the precipitation was also calculated at each longitude (Figure 2b). The regression coefficient, i.e., GW variance per precipitation, is particularly large near the longitudes of 40°E and again at 130°E where the African and Australian continents are respectively located. This fact suggests that convection over the continents generates more GWs with long vertical wavelengths which are easily detected by AIRS than that over the ocean.

3.1 Characteristics of the GW variance synchronized with the MJO

To quantify the variation of the GW variance in relation to the MJO, we use the RMM index [*Wheeler and Hendon*, 2004]. This index is defined by using the first and second principal components (RMM1 and RMM2) from the empirical orthogonal function (EOF) analysis of a combined field of daily outgoing long wave radiation (OLR) and zonal winds at 200 hPa and 850 hPa. The RMM index is classified into eight phases in which specific spatial patterns such as the location of the convective region is described. A low OLR region as an index of strong convection is located over Africa and the South Pacific in Phase 1, over the South Indian Ocean in Phases 2 to 4, over the Maritime Continent region in Phases 4 to 5, and over the western to central parts of the South Pacific in Phases 5 to 8 [*Wheeler and Hendon*, 2004].

Figures 3a and 3b respectively show the time series of the magnitude and phase of the RMM vector which is composed of RMM1 and RMM2. It is clear that the MJO migrates with two or three cycles in four months from December through March in most years. The eastward migrations of high precipitation and high GW variance regions (Figures 1a and 1b) correspond well with the progression of the RMM index.

Next, composite maps of the precipitation, GW variance around 3 hPa, and zonal winds at 100 hPa and 200 hPa were made as a function of the MJO phase. For the composite, only time periods with the RMM vector magnitudes greater than 1 were used. The number of days used for the composite and the number of all days are respectively shown by red and black curves as a function of the MJO phase in Figure 3c. More than 50 cases are used for the composite for respective RMM phases.

Figure 4 shows the composite maps of anomalies of the precipitation, GW variance, and zonal winds at 100 hPa from the mean for each of the eight RMM phases. Only regions with a confidence level greater than 90% are shown. The spatial distribution of precipitation is similar to that of the GW variance in all MJO phases. The high precipitation region and the high GW variance region similarly migrate eastward following the RMM phase progressions. These spatial distributions and time evolution are similar to that of the OLR shown by *Wheeler and Hendon* [2004]. Thus, it is likely that the GWs in the subtropical stratosphere are likely generated by convection varying with the MJO on intraseasonal time scales.

In Figure 4c, it is seen that zonal wind anomalies at 100 hPa are significantly westward in the regions with high precipitation and high GW variances in all RMM phases. *Kiladis et al.* [2005] showed that the zonal winds associated with the MJO are slightly tilted eastward with height in the upper troposphere. We also examined zonal wind at 200 hPa and found that the location of the westward wind anomalies at 100 hPa is similar to that at 200 hPa with a slight difference (not shown) as is consistent with Kiladis et al. Thus, the large westward wind at 100 hPa where the GW variance is large is a feature of the tropospheric circulation associated with the MJO.

3.2 Regulation of GWs penetrating into the stratosphere by the zonal wind around the tropopause

As already mentioned, there is regional correspondence between the GW variance around 3 hPa and the strong westward wind at 100 hPa. This feature is particularly evident in the longitude region of 60°E−120°W. In order to examine this point in more detail, we made the following analysis. First, zonal winds at 100 hPa, GW variance at 3 hPa, and precipitation are averaged over the region of 0°−20°S and for every 10 days at each longitude in a range of 60°E–120°W. Next, the zonal winds are binned and averaged according to GW variance at 3 hPa versus precipitation (Figure 5). Mean zonal winds are only shown in bins containing more than five data points. It is seen that the westward wind tends to be stronger for larger GW variance at all precipitation values. Regression coefficients of the mean zonal wind onto the GW variance were calculated for each precipitation bin of 2.5 mm day^{-1}. The increment of the GW variance per unit mean zonal wind at 100 hPa was in the range of −0.034 to −0.064 K^{2}m^{-1}s. This relation indicates that stronger westward wind around the tropopause is more preferable for generation and/or propagation of the GWs into the stratosphere. Moreover, if such a relation is due to critical level filtering, this result would suggest that many GWs generated by convection in association with the MJO have small or westward phase speeds in the range of -16 to +8 m s^{-1}, the range of zonal winds observed at 100hPa.

The precipitation, GW variance around 3 hPa, and mean zonal wind at 100 hPa have strong longitudinal dependence as shown in Figures 1 and 2. Thus, the relation observed in Figure 5 might be simply reflecting such longitudinal dependence. However, this is not the case. We performed a similar analysis on the anomalies of these quantities from their seasonal mean at each longitude, and a similar relation between the mean zonal wind and the GW variance as that shown in Figure 3 was obtained (not shown).

The results shown above suggest that there are two ways for the MJO to modulate the GW variance in the stratosphere. One is through GW generation from strong convection associated with the MJO. The other is through GW propagation in the zonal wind structure that is characteristic of the MJO.

4. Summary and concluding remarks

The intraseasonal variability of the GW variance around 3 hPa in the subtropical stratosphere was examined using high-resolution temperature data from AIRS for eight austral summers from December 2003 through March 2011. It was shown that the GW variance varies at periods of tens of days. The GW variance was enhanced in the region where high precipitation and relatively strong westward tropopause winds were present. Regions with large GW variance and precipitation both migrate eastward in association with the MJO.

This relation was more clearly and quantitatively shown by a composite analysis of the GW variance around 3 hPa, precipitation, and zonal wind at 100 hPa as a function of the MJO phases based on the RMM index. It was shown that the migration of the large GW variance region was closely related to the MJO's characteristic precipitation and upper tropospheric zonal winds. The results suggest that characteristic strong convection associated with the MJO is important as a source of GWs observed in the tropical stratosphere, and that the characteristic upper tropospheric westward winds associated with the MJO also regulates GWs penetrating into the middle atmosphere likely through critical level filtering.

It is noted that the upper tropospheric wind speed also controls generation of waves by an obstacle effect near the top of the convection. *Evan et al.* [2012] found evidence for the envelope of MJO convection as the source for a large-scale inertia-gravity wave event observed over the Maritime Continent. They further identified the upper tropospheric westward shear as important for generating this wave event. Although the horizontal wavelengths of gravity waves examined in their study were about 5000 km, which are much larger than those detected by AIRS observation, a similar obstacle-effect type of source generation of small horizontal-scale gravity waves may be important. Our results showing that tropopause winds are an important predictor of stratospheric gravity wave variance is also consistent with such GW generation by an obstacle effect, along with the critical wave filtering.

For further quantitative discussion, it is important to examine the generation and propagation of GWs related to the MJO with model experiments. *Horinouchi* [2008] examined modulation of GW excitation and propagation using a regional model and compared results for active and inactive phases of the MJO. His results indicated that upward GW propagation was significantly enhanced during the MJO inactive phase, especially for GWs with phase speeds greater than 20 m s^{-1}. In contrast, our observational study showed evidence of stronger GW activity in the stratosphere coupled with the MJO. An idealized model simulation may be useful to clarify this point.

In addition, it should be indicated that a comparison of GW characteristics measured by satellites with different observational filters is useful. AIRS, which is a nadir-viewing instrument, can observe a wide range of GW horizontal wavelengths but is sensitive only to GWs with long vertical wavelengths. On the other hand, limb-viewing or GPS radio occultation satellite instruments can observe a wide range of GW vertical wavelengths but are primarily sensitive only to GWs with long horizontal wavelengths. Combinations of different types of satellite observations allows us to examine the wide range of GW horizontal and vertical wavenumbers. Combining analysis from both types of measurements to examine relationships with the MJO would be interesting, but we leave this for future studies.

Another important implication of the results obtained by the present study is that the mesospheric circulation may have an intraseasonal variation because GWs modulated by the MJO can propagate deep into the middle atmosphere and deposit their momentum. It may also be important that these GWs exhibit significant longitudinal variations (e.g. *Eckermann et al.*, [1997]). It would be interesting to elucidate how the three-dimensional structure of the mesospheric circulation may be modified on intraseasonal time scales using recently derived theoretical formula by *Kinoshita and Sato* (2013a and 2013b). However, this issue is also left for future studies.

Acknowledgements. The authors acknowledges Yukari N. Takayabu, Masaaki Takahashi, Tomoki Tozuka, Hiroaki Miura, and Tomoe Nasuno for constructive discussions. This work is supported by JSPS KAKENHI Grant Numbers 24-2641 and 25247075. MJA was supported by the National Science Foundation grant #AGS-1519271. Figures were drawn using the GFD-DENNOU library.

References

Alexander, M. J., and C. Barnet (2007), Using satellite observations to constrain parameterizations of gravity wave effects for global models, *J. Atmos. Sci.*, *64*, 1652–1665, doi:10.1175/JAS3897.1.

Aumann, H. H., M. T. Chahine, C. Gautier, M. D. Goldberg, E. Kalnay, L. M. McMillin, H. Revercomb, and P. W. Rosenkranz (2003), AIRS/AMSU/HSB on the Aqua mission: Design, science objective, data products, and processing systems, *IEEE Trans. Geosci. Remote Sens.*, *41*, 253–264, doi:10.1109/TGRS.2002.808356.

Eckermann, S. D. (1997) Influence of Wave Propagation on the Doppler Spreading of Atmospheric Gravity Waves, *J. Atmos. Sci.*, 54, 2554–2573, doi:http://dx.doi.org/10.1175/1520-0469(1997)054<2554:IOWPOT>2.0.CO;2.

Evan, S., M. J. Alexander, and J. Dudhia (2012), WRF simulations of convectively generated gravity waves in opposite QBO phases, *J. Geophys. Res., 117,* D12117, doi:10.1029/2011JD017302.

Grimsdell, A. W., M. J. Alexander, P. T. May, and L. Hoffmann (2010), Model study of waves generated by convection with direct validation via satellite, *J. Atmos. Sci.*, *67*, 1617–1631, doi:10.1175/2009JAS3197.1.

Hecht, J. H., M. J. Alexander, R. L. Walterscheid, L. J. Gelinas, R. A. Vincent, A. D. MacKinnon, J. M. Woithe, P. T. May, W. R. Skinner, M. G. Mlynczak, and J. M. R. III (2009), Imaging of atmospheric gravity waves in the stratosphere and upper mesosphere using satellite and ground-based observations over Australia during the TWPICE campaign, *J. Geophys. Res.*, *114*, D18123, doi:10.1029/2008JD011259.

Hoffmann, L., and M. J. Alexander (2009), Retrieval of stratospheric temperatures from Atmospheric Infrared Sounder radiance measurements for gravity wave studies, *J. Geophys. Res.*, *114*, D07105, doi:10.1029/2008JD011241.

Hoffmann, L., and M. J. Alexander (2010), Occurrence frequency of convective gravity waves during the North American thunderstorm season, *J. Geophys. Res.*, *115*, D20111, doi:10.1029/2010JD014401.

Hoffmann, L., X. Xue, and M. J. Alexander (2013), A global view of stratospheric gravity wave hotspots located with Atmospheric Infrared Sounder observations, *J. Geophys. Res.*, *118*, 416–434, doi:10.1029/2012JD018658.

Horinouchi, T. (2008), A numerical study of upward-propagating gravity waves in two different MJO phases, *Geophys. Res. Lett.*, *35*, L17802, doi:10.1029/2008GL034992.

Huffman, G. J., R. F. Adler, M. M. Morrissey, D. T. Bolvin, S. Curtis, R. Joyce, B. McGavock, and J. Susskind (2001), Global precipitation at one-degree daily resolution from multisatellite observations, *J. Hydrometeor.*, *2*, 36–50, doi:10.1175/1525-7541(2001)002<0036:GPAODD>2.0.CO;2.

Jiang, J. H., B. Wang, K. Goya, K. Hocke, S. D. Eckermann, J. Ma, D. L. Wu, and W. G. Read (2004), Geographical distribution and interseasonal variability of tropical deep convection: UARS MLS observations and analyses, *J. Geophys. Res.*, *109*, D03111, doi:10.1029/2003JD003756.

Kiladis, G. N., K. H. Straub, and P. T. Haertel (2005), Zonal and vertical structure of the Madden-Julian Oscillation, *J. Atmos. Sci.*, *62*, 2790–2809, doi:10.1175/JAS3520.1.

Kim, S.-Y., H.-Y. Chun, and D. L. Wu (2009), A study on stratospheric gravity waves generated by Typhoon Ewiniar: Numerical simulations and satellite observations, *J. Geophys. Res.*, *114*, D22104, doi:10.1029/2009JD011971.

Kinoshita, T., and K. Sato (2013a), A formulation of three-dimensional residual mean flow applicable both to inertia-gravity waves and to Rossby waves, *J. Atmos. Sci., 70,* 1577-1602, doi:10.1175/JAS-D-12-0137.1.

Kinoshita, T., and K. Sato (2013b), A Formulation of Unified Three-Dimensional Wave Activity Flux of Inertia–Gravity Waves and Rossby Waves, *J. Atmos. Sci.*, *70*, 1603-1615, doi:10.1175/JAS-D-12-0138.1.

McLandress, C., M. J. Alexander, and D. L. Wu (2000), Microwave Limb Sounder observations of gravity waves in the stratosphere: A climatology and interpretation, *J. Geophys. Res.*, *105* (D9), 11,947–11,967, doi:10.1029/2000JD900097.

Okamoto, K., K. Sato, and H. Akiyoshi (2011), A study on the formation and trend of the Brewer-Dobson circulation, *J. Geophys. Res.*, *116*, D10117, doi:10.1029/2010JD014953.

Rienecker, M. M., M. J. Suarez, R. Gelaro, R. Todling, J. Bacmeister, E. Liu, M. G. Bosilovich, S. D. Schubert, L. Takacs, G.-K. Kim, S. Bloom, J. Chen, D. Collins, A. Conaty, A. da Silva, W. Gu, J. Joiner, R. D. Koster, R. Lucchesi, A. Molod, T. Owens, S. Pawson, P. Pegion, C. R. Redder, R. Reichle, F. R. Robertson, A. G. Ruddick, M. Sienkiewicz, and J. Woollen (2011), MERRA: NASA's Modern-Era Retrospective Analysis for Research and Applications, *J. Climate*, *24*, 3624–3648, doi:10.1175/JCLI-D-11-00015.1.

Sato, K., S. Watanabe, Y. Kawatani, Y. Tomikawa, K. Miyazaki, and M. Takahashi (2009), On the origins of mesospheric gravity waves, *Geophys. Res. Lett.*, *36*, L19801, doi:10.1029/2009GL039908.

Sato, K., C. Tsuchiya, M. J. Alexander, and L. Hoffmann, Climatology and ENSO-related interannual variability of gravity waves in the southern hemisphere subtropical stratosphere revealed by high-resolution AIRS observations, Submitted to *J. Geophys. Res.*

Stockwell, R. G., L. Mansinha, and R. P. Lowe (1996), Localisation of the complex spectrum: The S-Transform, *IEEE Trans. Signal Process.*, *44* (4), 998–1001, doi:10.1109/78.492555.

Watanabe, S., Y. Kawatani, Y. Tomikawa, K. Miyazaki, M. Takahashi, and K. Sato (2008), General aspects of a T213L256 middle atmosphere general circulation model, *J.*

Geophys. Res., *113*, D12110, doi:10.1029/2008JD010026.

Wheeler, M. C., and H. H. Hendon (2004), An all-season Real-time Multivariate MJO index: Development of an index for monitoring and prediction, *Mon. Wea. Rev.*, *132*, 1917–1932, doi:10.1175/1520-0493(2004)132<1917:AARMMI>2.0.CO;2.

Wu, D. L., P. Preusse, S. D. Eckermann, J. H. Jiang, M. de la Torre Juarez, L. Coy, and D. Y. Wang (2006), Remote sounding of atmospheric gravity waves with satellite limb and nadir techniques, *Advances in Space Research*, *37* (12), 2269 – 2277, doi:10.1016/j.asr.2005.07.031.

Yue, J., L. Hoffmann, and M. J. Alexander (2013), Simultaneous observations of convective gravity waves from a ground-based airglow imager and the AIRS satellite experiment, *J. Geophys. Res.*, *118* (8), 3178–3191, doi:10.1002/jgrd.50341.

Zhang, C. (2005), Madden-Julian Oscillation, *Rev. Geophys.*, *43*, RG2003, doi:10.1029/2004RG000158.

Figure captions

Figure 1. Time and longitude cross sections of (a) precipitation, (b) GW variance around 3 hPa (colors), and the zonal wind at 100 hPa as contours averaged over the latitudes from 0°S to 20°S and binned with an interval of 10° longitude and 10 days in the months from December to March of each year, where the +/-5 m s^{-1} contours are red/blue.

Figure 2. (a) Correlation coefficients of the time series of precipitation and GW variance as functions of longitude. A correlation coefficient of 0.27 (significance level of 99%) is shown as a thin vertical line. (b) Regression of the GW variance to precipitation.

Figure 3. (a) Time series of the magnitude of the RMM vector, which is composed of RMM1 and RMM2 of the RMM index (RMM vector, http://cawcr.gov.au/staff/mwheeler/maproom/RMM/). RMM vector magnitudes greater than 1 are plotted as red curves. (b) Time series of the phase of the RMM vector. The red color shows the region with RMM vector magnitude greater than 1. (c) (Black curve) Number of days used for the composite in Figure 5 in the respective phases of the RMM index. (Red curve) The same as the black curve but only for days with an RMM vector magnitudes greater than 1.

Figure 4. Composite maps of the anomalies of (a) precipitation, (b) GW variance, and (c) zonal winds at 100 hPa for the respective phases of the RMM index. Only the regions with a significance level greater than 90% are shown.

Figure 5. A scatter plot of the precipitation versus the GW variance around 3 hPa. Only bins in which the number of data is greater than five are colored. Colors show the mean zonal wind at 100 hPa at the respective bins in this diagram.

Figures

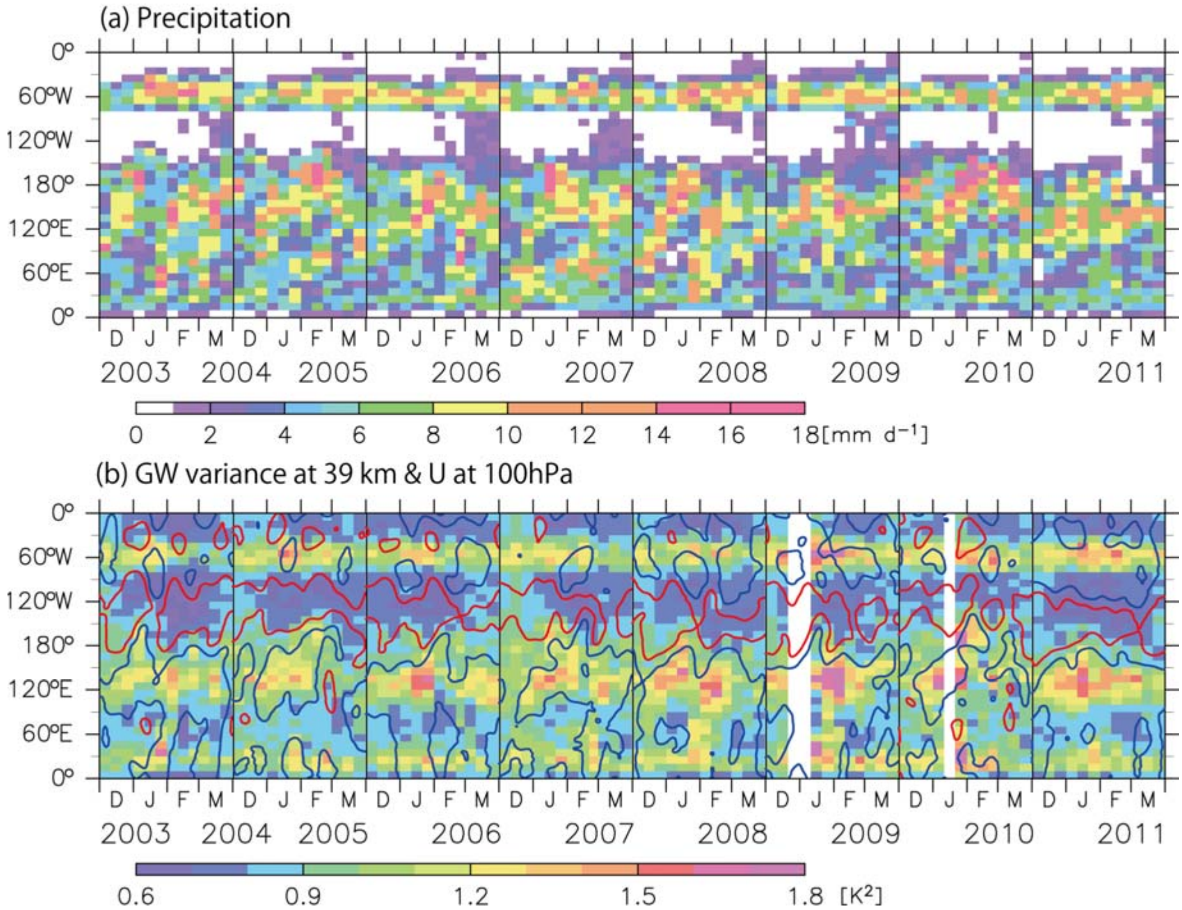

Figure 1. Time and longitude cross sections of (a) precipitation, (b) GW variance around 3 hPa (colors), and the zonal wind at 100 hPa as contours averaged over the latitudes from 0°S to 20°S and binned with an interval of 10° longitude and 10 days in the months from December to March of each year, where the +/-5 m s^{-1} contours are red/blue.

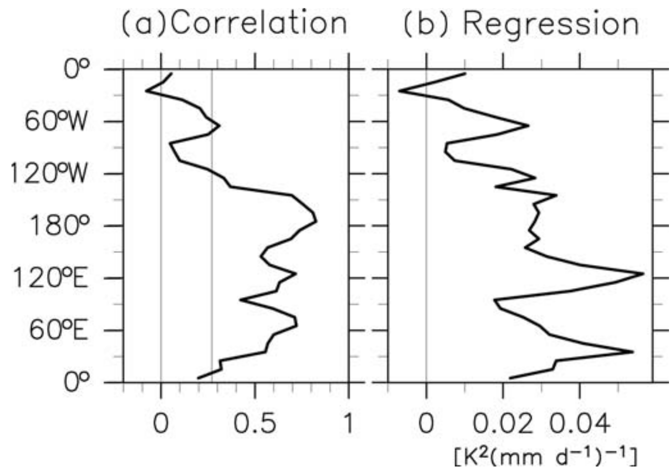

Figure 2. (a) Correlation coefficients of the time series of precipitation and GW variance as functions of longitude. A correlation coefficient of 0.27 (significance level of 99%) is shown as a thin vertical line. (b) Regression of the GW variance to precipitation.

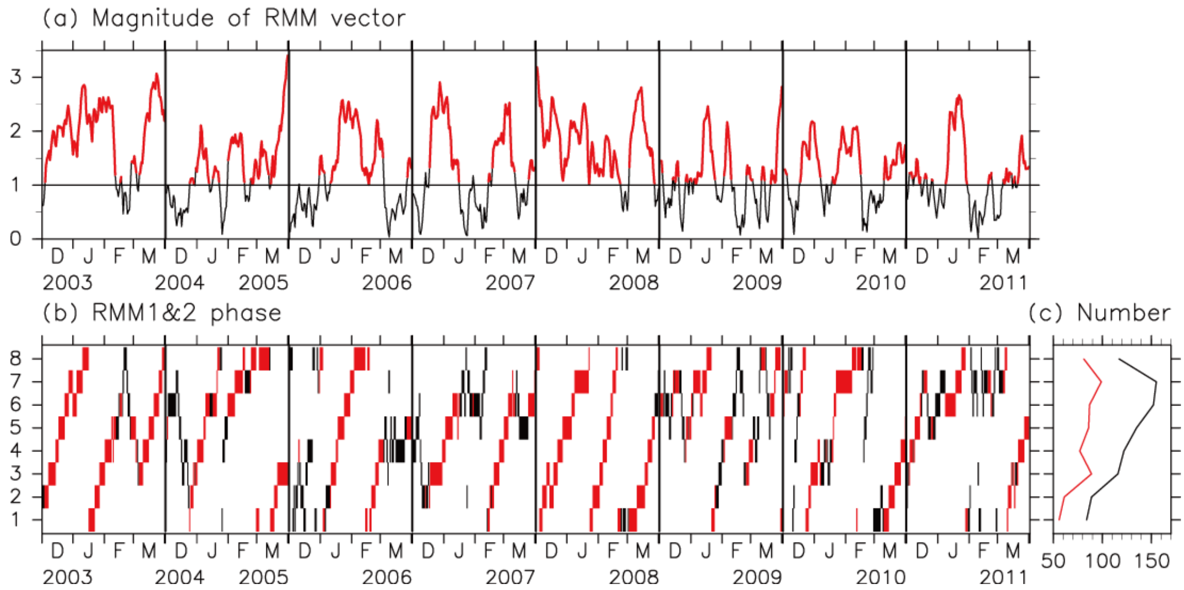

Figure 3. (a) Time series of the magnitude of the RMM vector, which is composed of RMM1 and RMM2 of the RMM index (RMM vector, http://cawcr.gov.au/staff/mwheeler/maproom/RMM/). RMM vector magnitudes greater than 1 are plotted as red curves. (b) Time series of the phase of the RMM vector. The red color shows the region with RMM vector magnitude greater than 1. (c) (Black curve) Number of days used for the composite in Figure 5 in the respective phases of the RMM index. (Red curve) The same as the black curve but only for days with an RMM vector magnitudes greater than 1.

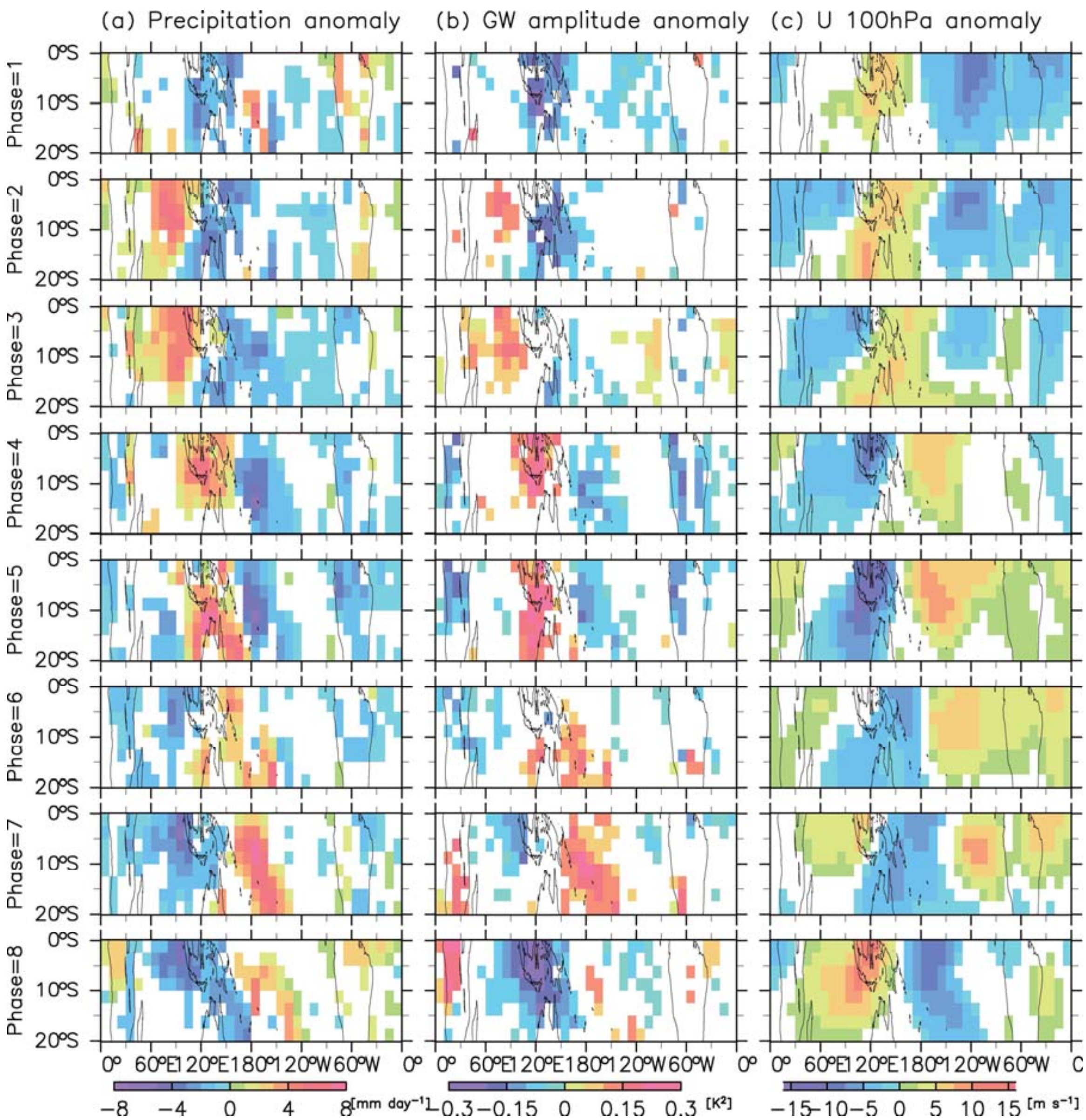

Figure 4. Composite maps of the anomalies of (a) precipitation, (b) GW variance, and (c) zonal winds at 100 hPa for the respective phases of the RMM index. Only the regions with a significance level greater than 90% are shown.

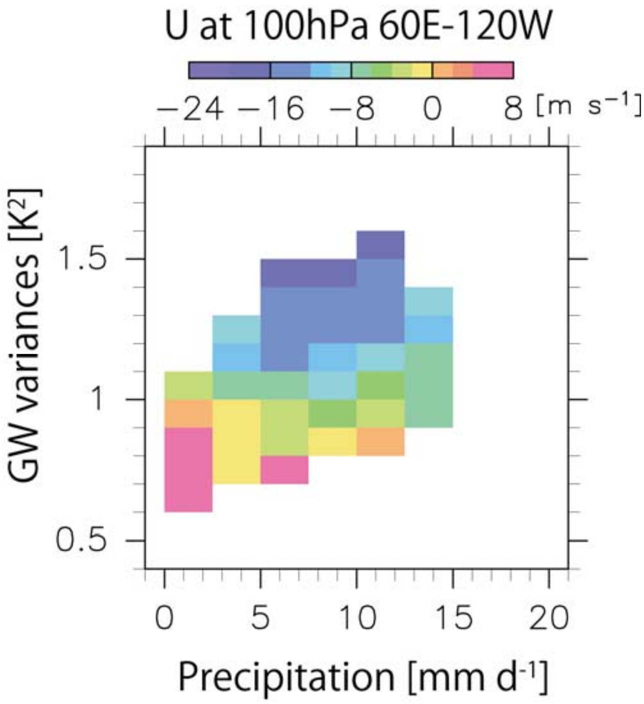

Figure 5. A scatter plot of the precipitation versus the GW variance around 3 hPa. Only bins in which the number of data is greater than five are colored. Colors show the mean zonal wind at 100 hPa at the respective bins in this diagram.